ACS APPLIED POLYMER MATERIALS

pubs.acs.org/acsapm Article

Effect of the Spin-Line Temperature Profile on the Translocation of the Solidification Point and Jet Thinning in Unconfined Melt Electrospinning

Elnaz Shabani, Amir Azimi Yancheshme, Avner Ronen, and Russell E. Gorga*

Cite This: *ACS Appl. Polym. Mater.* 2021, 3, 268–278 Read Online

ACCESS | Metrics & More | Article Recommendations | Supporting Information

ABSTRACT: This work aims to provide effective strategies and practical tools to control the diameter of fibers, a long-lasting challenge in the application of free surface melt electrospinning, mainly by highlighting the importance of the solidification point. A systematic approach to mapping the solidification point and temperature profile in an electrohydrodynamic jet in the melt electrospinning process was developed experimentally through the backlit imaging technique and numerically through computational fluid dynamics. The effect of the different spin-line temperature profiles on the robustness of the process as well as the fiber morphology was investigated. Scanning electron microscopy analysis demonstrated that at high spin-line temperature profiles, the fiber diameter dropped by four times compared to the room temperature spin-line environment. Both in situ backlit images from the jets in the spin line and the numerical phase fraction analysis revealed an immediate solidification of the jet, which is elongated twice in the case of the high spin-line temperature profiles. The elongated freezing length for the high spin-line temperature profiles as a result of the delayed solidification was identified as one of the main factors contributing to the jet thinning and subsequent fiber diameter reduction. Based on the simulation, the temperature profile of the jet demonstrated an approximately 20 °C drop along the jet length in the nonsolidified portion (freezing length), proposing the viscosity drop as a second factor in the fiber diameter reduction mechanism. Ultimately, the molten film thickness on the plate was identified as a semiphysical confinement parameter, controlling the size of the formed cones and subsequently the fiber diameter, despite the free surface nature of the unconfined melt electrospinning.

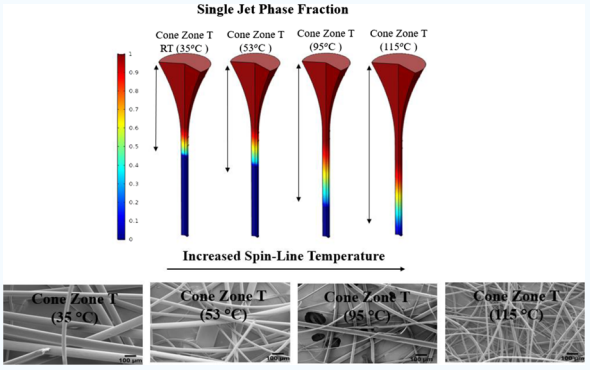

KEYWORDS: *unconfined melt electrospinning, solidification point, spin-line temperature profile, electrohydrodynamic jet, computational fluid dynamics*

1. INTRODUCTION

Electrospinning is a versatile technique for producing continuous fibers. A wide variety of polymers are viable to turn into fibrous structures of micro- to nanosize through electrospinning.[1] These sub-micrometer-scale structures possess an extensive surface area-to-volume ratio, which enables them to be used in a variety of applications.[2] Applications of nanofibers include biomedical,[3−5] textiles,[6] filtration,[7] and sensors.[8,9] The electrospinning technique, even though is simple with easy setup and straightforward to fabricate materials with advanced functions, has not yet become a potential source of fabrication for large-scale manufacturing. The low production rate has been a long-lasting bottleneck for this technique, which has recently become an emerging topic of investigation for researchers.

Yarin et al. (2004) introduced free surface electrospinning, which explored the potential of the electrospinning technique for upscale and high production rate purposes.[10] In their first trial, both electrical and magnetic fields were utilized as driving forces acting on a two-layer system. They observed that several cones form on the free surface of the fluid, increasing the production rate 12-fold as well as eliminating the frequent clogging problem in traditional electrospinning setups. Lukas et al. explained the theoretical concept of the self-organization of the jets from the free surface of a one-dimensional liquid.[11] The phenomenon is explained by the initial wave formation on the free surface of the liquid, following by the domination of the "fastest forming instability" at a certain electric field that creates the so-called perturbation or cones. The insightful knowledge of the fundamentals of free surface electrospinning

Received: September 27, 2020
Accepted: December 7, 2020
Published: December 17, 2020

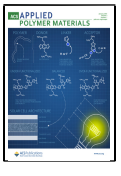

https://dx.doi.org/10.1021/acsapm.0c01082
ACS Appl. Polym. Mater. 2021, 3, 268–278

has facilitated many interventions on the setup design for the technique.[12−19] Many of the current free surface designs use a polymer solution to fabricate fibers.

Solution electrospinning, despite the popularity, encompasses various challenges, including the usage of toxic solvents, low production rate, presence of residual solvents in fiber, and the limitation to be employed in thermoplastics, like polyolefins, that do not readily dissolve in a solvent at room temperature.[20] Melt electrospinning, which utilizes the polymer melt directly as a spinning fluid, has gained popularity in recent years. This green approach provides versatility for thermoplastic fiber fabrication, offers sustainability by elimination of the toxic solvent, and enhances the overall throughput.[21,22] The recently introduced free surface melt electrospinning overcomes the challenges associated with the pumping of the high-viscosity polymer melt through a tiny needle and increases the viability of the technique for industrial upscaling. The first configuration was proposed in 2010, called rod electrospinning, in which the polymer is fed on top of a rod electrode and after melting, self-organization of multiple jets on the free surface of the rod produces spinning jets.[18] Several more designs of free surface electrospinning have been proposed that even though meets the essential shortcomings of the melt electrospinning technique yet suffers from difficulty in the feeding mechanism or complexity of the design.[15,23] Melt electrospinning from a plate surface, developed in 2014 by Gorga and Clarke et al., is a simple approach for fabricating micrometer-scale fibers.[24] Due to the high-viscosity nature of the polymer melt and the lack of whipping motion, fibers obtained from this technique are shown to have larger diameters than those from the solution techniques. Therefore, further thinning optimization is required to obtain fibers with size ranges comparable to their solution-spun counterparts. Many researchers have identified that the main factor affecting the jet thinning is the viscosity, which is normally controlled by temperature. However, Naraghi et al. observed a reverse dependence of fiber diameter to melt viscosity for free surface melt electrospinning, attributed to the viscosity-dependent flow rate in this method. The effects of the spin-line temperature, the temperature of the surrounding air around the spinning jet, on the morphology of the fibers have been studied before. This was obtained by the utilization of extra heating modules in the spin-line region, which could complicate the setup design further. The further thinning of the fiber by increasing the spin-line temperature is attributed to the decreased viscosity of the jet and, as a result, the enhancement of the stretchability.[25,26] Joo et al. utilized an infrared camera to tentatively monitor the inside jet temperature and observed rapid jet quenching, faster than model predictions, which was linked to electrohydrodynamic effects.[27]

Achieving sub-micrometer-scale fibers from melt-phase spinning processes, including melt electrospinning, has been a long-lasting challenge. To date, there is no study that fundamentally investigates the essence of the solidification or phase-change process in an electrospinning jet and its correlation with further thinning of the jet and the final fiber diameter. In this work, a backlighting technique, developed by the authors,[28] was utilized to precisely determine the solidification point in a melt electrospun jet. The electrospinning jet was considered as a phase-change material that undergoes solidification to become a fiber. This concept became the basis for the utilization of the computational fluid dynamics, introduced as a practical tool to monitor the jet behavior in a melt-phase electrospinning process. The approach here is unique because it introduces a systematic method to precisely control the spinning zone temperature without the need to increase the melt temperature or incorporate any second-part heating module along with a real-time monitoring tool. The strategies and tools are in particular discussed for the relatively new field of free surface melt electrospinning; however, it should translate to other melt-phase fiber fabrication techniques.

2. EXPERIMENTAL SECTION

2.1. Materials. In this work, a linear low-density polyethylene (PE) granule was used for all experiments. PE, ASPUN 6850 fiber-grade resin, with a melt index of 30 g/min under 190 °C/2.16 kg based on the data sheet provided by the manufacturer, was supplied by Dow Chemical company. PE powder was obtained with a cryogenic grinder using a freezer mill grinder, and SPEX CertiPrep 6750 was purchased from SPEX SamplePrep. PE powder was used to create a uniform molten film on the plate. The melting temperature of this PE (T_m), based on the obtained differential scanning calorimetry thermogram, is 129 °C.

2.2. Apparatus. The unconfined melt electrospinning apparatus (Figure 1) consists of an aluminum sharp edge plate with a surface

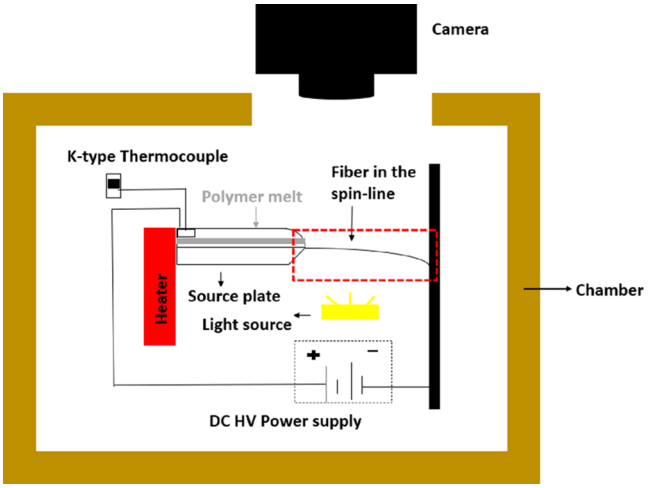

Figure 1. Schematic of the apparatus inside the chamber from side view accompanied by a backlighting camera setup.

area of 13.6 × 4.8 cm and edge walls of 1 mm thickness and 0.8 cm height on the sides (with no wall on the sharp edge where fibers are formed). As aluminum has a low abrasion resistance, to get a consistent sharpness in the spinning edge of the plate that undergoes heavy cleaning after each run of the process, a steel blade was cut and screwed in on to the edge. A commercial hot plate (Fisher Scientific, model: HP88857100) was used to heat up the source plate in two modes: in the first mode, the source plate is placed on the hot plate off-centered where the edge of the plate protrudes by 2 cm. In the second mode, the source plate is attached to the hot plate from the back wall and the entire plate protrudes (Figure 2). The two modes provide the spin-line environment with different temperature profiles that are discussed in more detail in Section 2.4. In both modes, the entire apparatus is placed in a wood chamber with a transparent front door and the top wall made of acrylic to observe the process. Thermal grease (Halnziye HY880) was used between the source plate and the hot plate for better thermal contact. One side of the source plate is connected to a K-type thermocouple to monitor the temperature of the source plate. The opposite side of the plate is attached to ground wire. The counterelectrode consists of a square aluminum plate with a surface area of 30 × 30 cm, which is connected to the negative

https://dx.doi.org/10.1021/acsapm.0c01082
ACS Appl. Polym. Mater. 2021, 3, 268−278

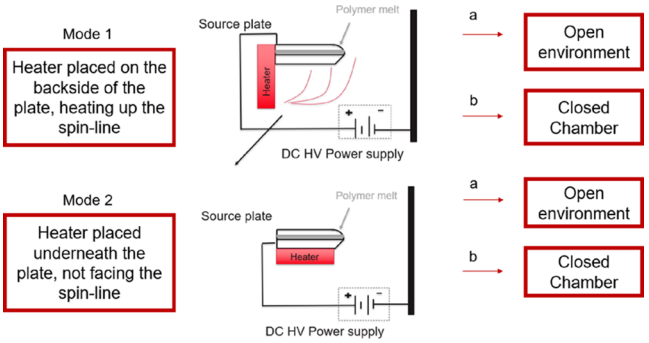

Figure 2. Schematic of the different modes of configuration; mode 1-a (open environment, vertical heater), mode 1-b (closed chamber, vertical heater), mode 2-a (open environment, horizontal heater), and mode 2-b (closed chamber, horizontal heater). Each mode provides a different spin-line temperature profile (Section 2.4).

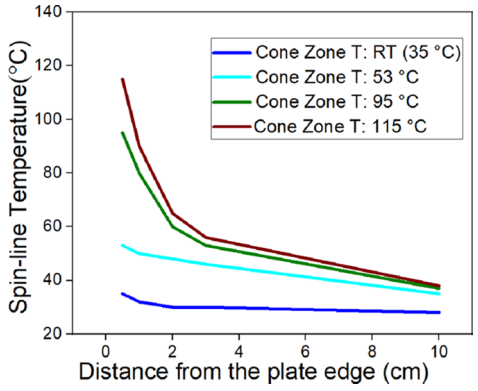

Figure 3. Spin-line temperature profiles specified by their cone-zone temperatures. Profiles are related to their respective configuration as Cone-Zone T: 115 °C relates to mode 1-b, Cone-Zone T: 95 °C relates to mode 1-a, Cone-Zone T: 53 °C relates to mode 2-b, and Cone-Zone T: RT relates to mode 2-a (mode configurations are shown in Figure 2).

polarity of a high voltage source (Glassman, Model FC60R2). A hand-made thermocouple holder is placed inside the chamber to measure the inside melt temperature before and after each run.

2.3. Experimental Characterization. All the spinning experiments were carried out at an electric field of 1.84E6 V/m at 500 microns away from the plate edge. Simulations were carried out using Ansys Maxwell software version 19.2. Voltages were set to 40 kV for the mode 1 and 32.7 kV for the mode 2 configuration to obtain the same electric field magnitude, as the simulation showed that the plate protrusion affects the electric field around the edge, which can result in different electric fields for the two modes. More information regarding the electric field simulation is provided in the Supporting Information (Figure S1 and Table S1). The spinning distance was set to 10 cm. The source plate was set to 190 °C due to which the temperature of the molten film on the plate reaches 165 ± 2 °C and remained almost constant throughout the running process for all the experiments with +2 °C increase after 20 min, which is assumed to be negligible. A camcorder (Canon, Model HF R72) was used to record the spinning process (run for 20, 40, and 70 min) for further analysis of jet evolution after the process. Still images were taken using a Canon DSLR camera (Canon EOS Rebel T5i with 18−135 mm EF-S IS STM Lens) for cone diameter and interjet spacing analyses using the ImageJ software. Each experiment was repeated three times, and the averaged results were reported. The backlighting technique was developed to obtain high-resolution images with clear object edges.[28] In this technique, a wireless portable LED lamp (33 LED Super Bright Wardrobe Lights, Portable Magnetic Stick Wireless, geometry 9.5 inch by 1.5 inch by 0.7 inch, manufacturer: CHNXU) was placed in the spinning region shining the camera lens directly with the spinning jets located between the camera and the lighting source (Figure 1). The process began with heating up the source plate to 190 °C and after the temperature of the plate was steady, 10 g (except for where noted) of the polymer powder was uniformly spread on the plate. When the source plate temperature became steady at 190 °C (experimentally, this was obtained after 15−20 min), the temperature of the molten polymer film was measured by inserting a thermocouple inside the melt. Lastly, a high voltage is applied between the source plate and the collector and electrospinning starts after the induction time is reached. The induction time is the time for the waves to reach the critical growth factor to maintain the formed waves on the surface of the fluid beyond the critical electric field and turn in the perturbations.

2.4. Spin-Line Temperature Profile. Four spin-line temperature profiles were obtained through different configuration designs (Figure 2) and were measured by inserting a thermocouple at 0.5, 1, 2, 3, and 10 cm distance from the plate edge, in the spin line (Figure 3). Cone zone, defined as the region 0.5 cm from the plate edge in the spin line, is where cones are initiated after ejecting from the plate. As the cone-zone temperature is an important feature of each spin-line temperature profile (due to the nonsolidified nature of the jet in this region that is discussed later in more detail), in this work, spin-line temperature profiles were described by their cone-zone temperature (e.g., the cone-zone temperature of RT (room temperature, 35 °C) refers to the dark blue curve shown in Figure 3).

It was observed that the temperature is almost uniform throughout the 13.6 cm length of the plate (from left to the right side) and only changes through the spin line, the path that the fiber travels after ejecting from the plate to reach the collector, as is specified by the spin-line temperature profiles. The hot plate is the main source of thermal heating for both the source plate and the spin line. The farther away from the hot plate into the spin line, larger the drop in temperature to lower degrees, as observed in the profiles. Another factor changing the temperature profile is the configuration of the hot plate. In the vertical mode (1-a and 1-b), the spin-line region was directly exposed by the hot plate and was heated up through the convection mechanism. In the case of a horizontal configuration, (2-a and 2-b), the spin-line region was less exposed by the hot plate and therefore was not directly being heated up; hence, a different profile was obtained.

2.5. Fiber Characterization. The fiber mat morphology was characterized using a scanning electron microscope (SEM) (Hitachi S3200N Variable Pressure SEM) at an accelerating voltage of 5 kV. The fibers were coated using a sputter coater with Au−Pd with a thickness of approximately 50 nm to form a conductive surface. To analyze the fiber diameter from the SEM images, the ImageJ software was used. For each sample, approximately 50 fibers were analyzed using at least three SEM images from different samples, and the average fiber diameter and standard error were reported.

2.6. Numerical Modeling and Simulation. A comprehensive numerical approach was applied in order to describe the phase-change process of the polymer melt in the electrospinning process. Heat and momentum transport equations along with continuity equations (eqs 1−3) were numerically solved using the finite element method to describe the fluid flow and temperature gradients throughout the fiber jet. Zero shear rate viscosity of polyethylene at the experimental temperature was experimentally measured and substituted in the momentum equation. This was also in line with other researchers' approach for the modeling of the melt electrospinning jet.[26,27] As the system is a continuous process, the steady-state model was utilized. All simulations were performed in a 2D axisymmetric framework with the aid of commercial code COMSOL Multiphysics 5.5.

Momentum transport equation

$$\rho(u\cdot\nabla)u = -\nabla p + \mu\nabla^2 u \quad (1)$$

Continuity equation

$$\nabla\cdot u = 0 \quad (2)$$

Heat transport equation

https://dx.doi.org/10.1021/acsapm.0c01082
ACS Appl. Polym. Mater. 2021, 3, 268−278

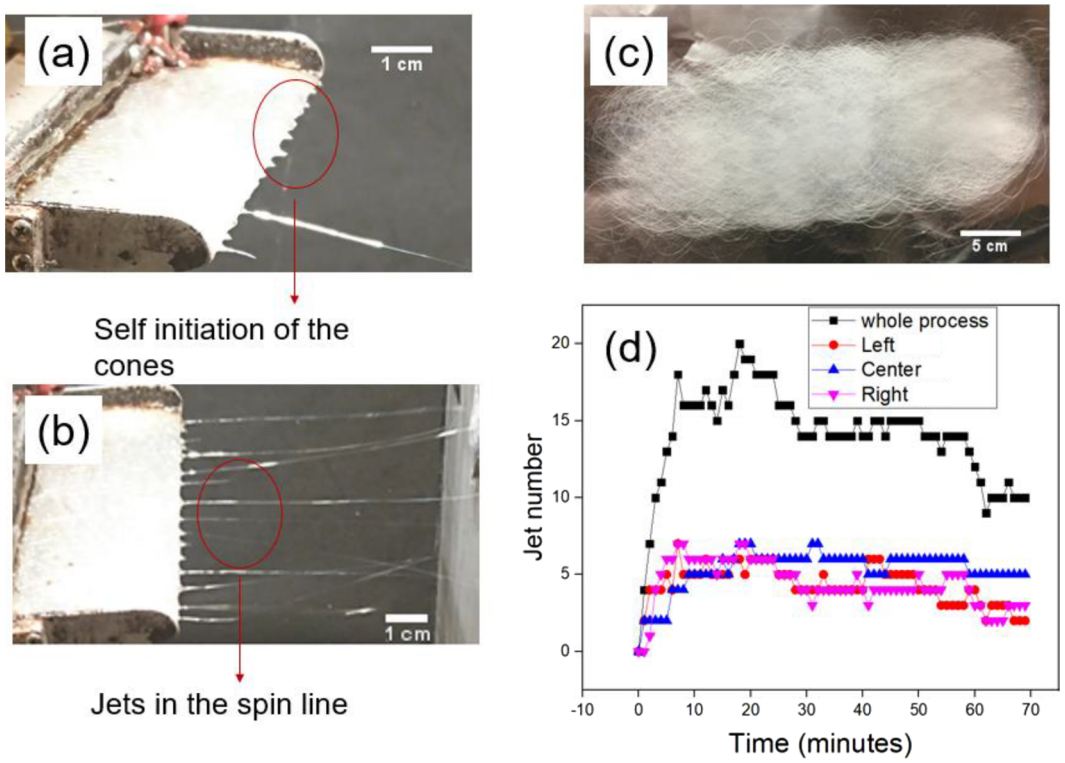

Figure 4. Illustration of the electrospinning process for (a) self-initiation of the cones, (b) in process view of the spinning jets, and (c) final product. The electrospinning parameters are set as 10 cm distance between the plate and the collector, 32.7 kV voltage, and the mode 1-a setup configuration with a cone-zone temperature of 95 °C; (d) jet evolution of electrospinning at 40 kV and a cone-zone temperature of 53 °C for 70 min run of the process. Analysis is done for the entire plate (black curve) as well as the middle, right, and left sections of the plate (colored curves).

$$\rho c_p u \nabla T = K \nabla^2 T \tag{3}$$

where p is the pressure, ρ is the density (kg/m^3), and k is the thermal conductivity (W/m·K), which is assumed to be constant in the melt electrospinning process,[26,27] C_p is the specific heat capacity at a constant pressure (J/kg·K) and u is the velocity of the polymer jet. Table S2 (Supporting Information) lists the material properties and operational conditions used in simulations, which are the same as our experimental conditions. Simulations have been carried out for the four different cases of spin-line temperature profiles categorized based on the surrounding air temperatures as shown in Figure 3.

In order to take the phase-change process into account, instead of using the latent heat directly into the energy balance equation, the apparent heat capacity formulation was used.[29,30] In this formulation, to account for the latent heat related to the phase transition, the phase of the material in the "mushy" zone (i.e., the region of both solid and molten materials coexists in the temperature interval of $T_m - {}^{\Delta T}/_2$ and $T_m + {}^{\Delta T}/_2$) is modeled using a smoothed function, θ, representing the fraction of the phase before the transition. The density (ρ), thermal conductivity (k), and the specific heat capacity (C_p) of the material are predicted as below (eqs 4−6)

$$\rho = \theta\rho_1 + (1 - \theta)\rho_2 \tag{4}$$

$$k = \theta k_1 + (1 - \theta)k_2 \tag{5}$$

$$\rho C_p = (\theta\rho_1 C_{p1} + (1 - \theta)\rho_2 C_{p2}) + \rho L_m {}^{d\alpha_m}/_{dT} \tag{6}$$

Indices 1 and 2 denote phase 1 (liquid) and phase 2 (solid), respectively. The first term of eq 6 represents the equivalent specific heat capacity where θ represents the melt fraction and the second term is the distribution of the latent heat. L_m is the latent heat and α_m is the mass fraction, which is defined by eq 7.

$$\alpha_m = {}^{(1 - \theta)\rho_2 - \theta\rho_1}/_{2\rho} \tag{7}$$

Heat transfer of the fiber jet with the surrounding air was modeled through convective heat transfer using the heat transfer coefficient (h) and the surrounding air temperature of the spin line ($T_{sur.}$) as specified in Figure 3 profiles. An empirical relation by Matsuo and Kase[31] was used to predict the heat transfer coefficient (eq 8). The adopted boundary conditions in this model are shown in Table S3 and Figure S2a (see Supporting Information).

$$h = 0.388 k_{air} ({}^{v}/_{\vartheta_{air}} \cdot A)^{0.334} (1 + ({}^{8v_{air}}/_{v})^2)^{0.166} \tag{8}$$

where h is the heat transfer coefficient, k_{air} is the air thermal conductivity, V is the fiber velocity, v_{air} is the surrounding air velocity, A is the cross-sectional area of the fiber, and ϑ_{air} is the kinematic viscosity of the air.

In order to resolve the location of phase transformation precisely, as it is not known at the first place, we started our simulations with a fine mesh (free triangular, 73,556 elements) along with an adaptive mesh refinement algorithm (i.e., refining the mesh to put more elements around the transition region) to rebuild meshes up to three adaptations. Figure S2b,c (Supporting Information) shows incorporated meshes before and after adaptation along with the geometry for the boundary condition.

3. RESULTS AND DISCUSSION

3.1. Jet Evolution. The spinning process starts with the self-initiation of the cone-shaped protrusions on the free surface of the polymer melt (Figure 4a). This phenomenon is recognized as self-organization based on the fastest forming instabilities. The interaction between the electric field force and the surface tension of the fluid causes instantaneous perturbation formation, which starts the electrospinning process (Figure 4b). The protrusions turn into spinning jets moving toward the collector and finally lay down on the collector as fibers (Figure 4c).

https://dx.doi.org/10.1021/acsapm.0c01082
ACS Appl. Polym. Mater. 2021, 3, 268−278

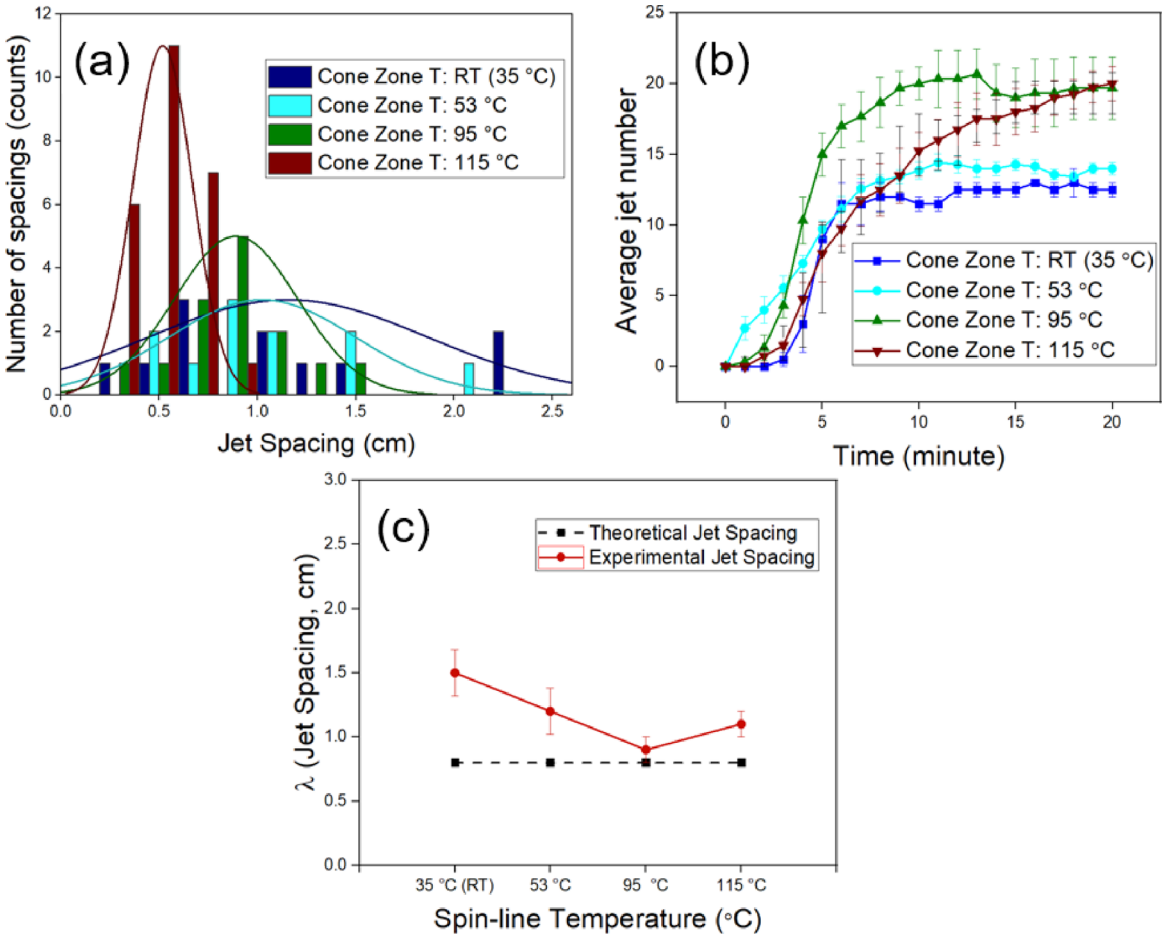

Figure 5. (a) Histogram of the jet spacing analysis of the 20 min run of the experiment for different spin-line temperature profiles, (b) Average jet number evolution for the first 20 min of the experiment, and (c) theoretical and experimental average jet spacings over the 20 min run of the experiment for different spin-line temperature profiles.

The jet number evolution with time is shown in Figure 4d for different run times. It is observed that the jet number evolution with time follows a growth function and levels off approximately after 15−20 min. The total number of jets levels off when the interjet distance saturates. As this saturation occurs after the 15 to 20 min run of experiments, all the experimental analyses are carried out on the products for a 20 min experiment run. The jet number analysis has been carried out by dividing the source plate into three sections. It is observed that all three sections of the plate (right, center, and left) show the same trend of jet evolution. This observation proves that the effect of side edges on the electric field is negligible in the spinning process.

3.2. Fabrication of Sub-micrometer Fibers. An important parameter in melt electrospinning that affects the fiber diameter is melt viscosity, which is inversely proportional to the temperature. Increasing the polymer melt temperature well above the melting point can lower the viscosity of the melt; however, prolonged exposure to high temperatures can cause chain scission and degradation.[32] Therefore, a higher temperature in the spin-line region, where jets enter after leaving the source plate, prevents spontaneous freezing of the jets, providing more stretching and a lower fiber diameter. In the following section, four different spin-line temperature profiles are examined and their effects on the solidification point and ultimately the fiber morphology and other process properties are described.

3.3. Evolution of the Jet Number and Jet Spacing with the Spin-Line Temperature. The distance between two adjacent jets was calculated experimentally by analyzing the static photo of the process taken after 20 min. The experimental results demonstrate that at higher spin-line temperatures, the average of jet−jet spacing decreases and it follows a narrower distribution. At higher spin-line temperatures, the average number of jets are also higher (Figure 5a,b). The narrower distribution of the spacings at higher spin-line profiles suggests that at a more crowded plate, jets are likely to be more organized compared to an empty surface where jets can localize more arbitrarily. The initial formed waves are the result of the interaction of the electric field and the surface tension on the surface of the fluid. Even though the melt temperature was kept constant despite the change in the spin-line temperature, one might assume that the melt surface on the edge of the plate where cones are formed is exposed to lower temperatures in case of lower spin-line profiles, which can affect the surface tension. Hence, it is noteworthy to recognize the possibility of the change in the surface tension of the polymer melt at different spin-line profile settings. As an estimation, the surface tension was calculated for the formed cones (perturbation) as they are a good representative of the melt surface at the edge of the plate. To estimate the temperature of the perturbations, the temperature profile throughout the entire jet, both on the surface and inside of the

https://dx.doi.org/10.1021/acsapm.0c01082
ACS Appl. Polym. Mater. 2021, 3, 268−278

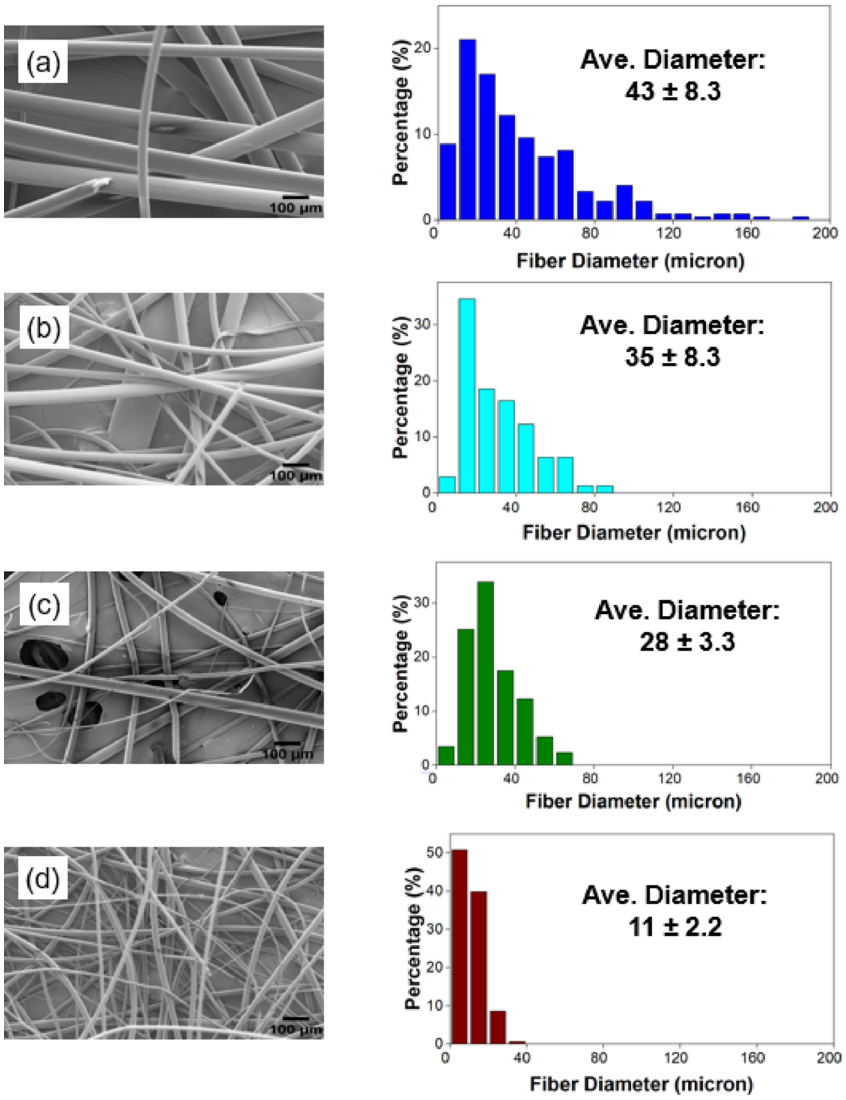

Figure 6. SEM images, fiber diameter distribution, and the reported measured fiber diameter for spin-line temperature profiles of (a) RT (35 °C), (b) 53 °C, (c) 95 °C, and (d) 115 °C.

jet, was numerically calculated using COMSOL simulation, which was discussed in more detail in Section 2.6.

The experimental average jet spacing was calculated by dividing the plate length by the average number of jets, which was calculated by analyzing the recorded process over the 20 min run of the experiment (the recorded process is reported in Figure 4d). The theoretical jet spacing was calculated using eq 9.[11]

$$\lambda = 2\pi(3\gamma/2\varepsilon_0 E^2) \tag{9}$$

where λ is the jet spacing, ε_0 is the permittivity of the free space, and γ is the surface tension and is calculated based on the equation from reference[33] (γ = 33.1−0.0390*T (°C) mN/m). Temperatures are calculated from the simulation on the surface of the cones (discussed in more detail in section 2.3) and are reported in Table S4 (Supporting Information). The electric field value 500 microns away from the plate edge, which is a good estimation of where cones are formed and start to turn into jets, is calculated based on the electric field simulation and is 1.8E6 V/m. Based on the simulation, the change in the jet surface temperature was relatively minimal, which is shown not to affect the surface tension of the melt at different spin-line profiles. The experimental average jet−jet spacing is approximately within the range of the theoretical calculated spacing and at higher temperatures with closer packing of the jets, the experimental results are closer to the theoretical data as shown in Figure 5c.

Figure 6a−d shows the effect of the spin-line temperature profile on fiber morphology and diameter. By increasing the spin-line temperature from RT to the 115 °C temperature profile, the average fiber diameter decreases from 43 microns to 11 microns. Based on the SEM images, the uniformity of the morphology significantly enhances at higher spin-line temperatures.

To analyze the fundamental effect of the spin-line temperature on lowering the fiber diameter, two hypotheses were proposed and evaluated. In the first hypothesis, the role of the spin-line temperature on reducing the size of the formed cones (perturbations) was evaluated. As observed in the jet spacing analysis, at high temperature profiles, more cones and jets are formed. This observation suggests that as more cones are formed on the free surface of the melt, less space might be available for the newer cones to form; hence, either smaller cones will be initiated or cones will shrink throughout the

https://dx.doi.org/10.1021/acsapm.0c01082
ACS Appl. Polym. Mater. 2021, 3, 268−278

process. To test this hypothesis, static photos taken from the process both at the initiation of each cones and after 20 min run of the experiment were examined, and cone diameters were measured and are reported in Figure S3a,b. Based on the observations, the average cone diameter does not show a trend with the cone-zone temperature. This was expected as the cones (protrusions) are formed due to the interaction between the electric field and the surface tension (eq 9) on the free surface of the fluid and viscosity (as an interrelated fluid parameter with the temperature) is not a factor. Moreover, the inside melt temperature and as a result the viscosity is kept constant in between all experiments and only the spin-line temperature is varied. However, on increasing the temperature, a narrower distribution of the cone diameter is obtained at the initiation stage. This is explained by the higher crowds of cones (or jets) at higher spin-line temperatures (Figure 5b), which is assumed to help with the uniform nucleation (initiation stage) of the cones on the free surface of the melt.

The second hypothesis regarding the mechanism of the fiber diameter reduction at higher spin-line temperature profiles is the solidification length throughout the jet. It is expected that at higher spin-line temperatures, the jet not only experiences a higher temperature and lower viscosity, but also goes through a greater amount of stretching due to the delayed solidification in the spin line. The stretching force on the jet is only effective on the thinning of the jet when applied to the melt portion of the jet as the solidified portion does not provide any significant chain mobility. To evaluate this, static photos were taken from the process utilizing the developed backlighting technique. This technique provided a means to take high quality in situ images from a micron scale object and revealed information regarding the phase change of the jets during the electrospinning process, which was previously unattainable. The freezing point (the phase-change location) is identified by the transformation of the transparent liquid jet into an opaque solidified jet (Figure 7a,b). In this work, the distance between the plate edge and the solidification point is defined as the freezing length. The freezing length was calculated for 15 distinct jets for each of the four different spin-line profiles. It was observed that at a high spin-line temperature (115 °C), the freezing length is longer than those at lower temperature profiles. It is worthwhile to mention that the cone diameter affects the size of the formed jet and consequently the jet's solidification process, as larger protrusions of the polymer melt take longer time to solidify. To solicit the effect of the cone size, the freezing length of the jet is normalized by its cone diameter (D_c) and the result is reported as the freezing length ratio (eq 10) in Figure 7c.

$$\text{Freezing Length} = {}^{\text{FL}}\!/_{D_c} \tag{10}$$

Based on the results, the freezing length ratio and the freezing length for the 115 °C profile are almost two times higher than the RT profile. The delay in the solidification provides a room for further stretching of the jet in the spin line and can directly affect the fiber diameter. In the next section, the freezing length was further validated through computation fluid dynamics simulation. Moreover, the temperature profile of the spinning jet was calculated to monitor the temperature and as a result the viscosity change throughout the length of the jet.

3.4. Computational Fluid Dynamics Simulation. The phase-change process of the jet through heat transfer with the spin-line environment is simulated based on the computational fluid dynamics approach. Figure 8a shows the liquid-phase fraction of the jet throughout the spin line for the four different spin-line profiles. It is observed that the phase change starts at a relatively short distance from the cone for all the cases (deviation after 1 cm in the graph of Figure 8a) and the solidification process is approximately completed within the first 1.5 cm of the jets (Figure 8b) (2D images are provided in the Supporting Information Figure S4). Based on experimental results obtained from both backlit images and simulation, the length of the liquid fraction is relatively small compared to the full length of the jet (1.5 to 10 cm), which highlights the limited accessibility of the fluid portion to undergo extensive stretching via an electric force. This can also justify the absence of the whipping motion in the melt electrospinning process, as the major portion of the jet exists in the solid phase. The shortage of the stretchable fluid phase in the jet dictates the importance of the role of the freezing length on the final fiber diameter.

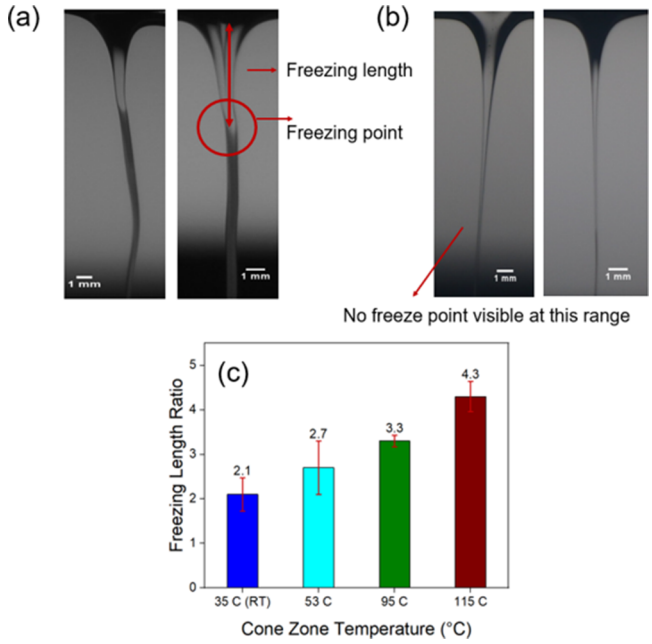

Figure 7. Illustration of the freezing point and freezing length through the jets recorded in situ using the backlighting technique for (a) RT spin-line profile and (b) 115 °C spin-line temperature profile. (c) Freezing length ratio calculated for the different spin-line temperatures profiles.

The backlit images revealed a longer freezing length of approximately 1.5 cm for the jets in the highest spin-line temperature profile (115 °C) compared to the 0.7 cm in the lowest temperature profile (RT). The results of the simulation and its comparison with the corresponding experimental data are presented in Figure 9a,b. Freezing lengths of the jets for each case of the spin-line temperature profiles were chosen and compared to the simulation results for further validation. Deviation of the model's prediction results from the experiment for all cases (Table 1) shows that both are in good agreement. The results from the simulation further validated the observation of the solidification point and the longer freezing length of the higher spin-line profiles. Higher deviation of the simulation results from the experiment is observed for the case of 95 and 115 °C profiles compared to the two lower temperature profiles. This is attributed to the

https://dx.doi.org/10.1021/acsapm.0c01082
ACS Appl. Polym. Mater. 2021, 3, 268−278

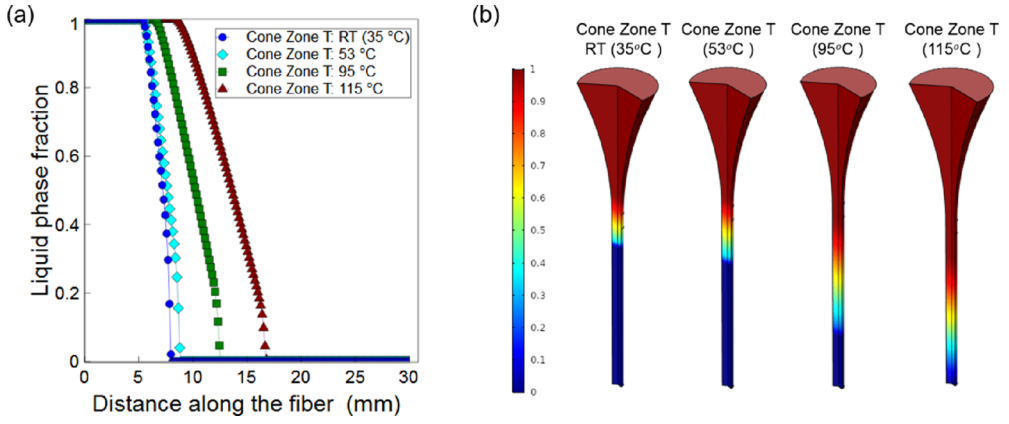

Figure 8. (a) Variation of the liquid-phase fraction along the fiber for different spin-line temperature profiles and (b) 3D phase fraction distribution inside fiber jets. Picture shows the first 15 mm distance from the cone of fibers.

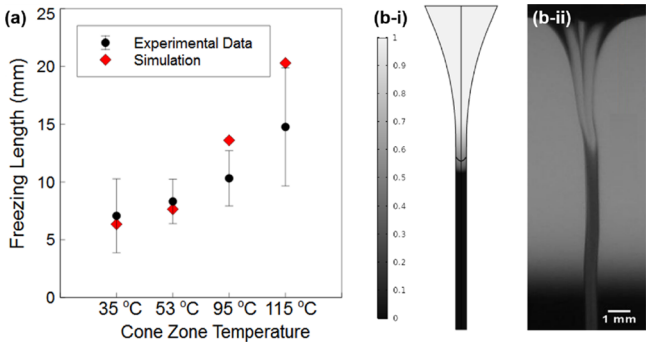

Figure 9. Experimental vs simulation results. (a) Values of freezing front for different air temperatures and (b) snapshot of freezing front for case 1; (b−i) simulation and (b−ii) experiment.

Table 1. Predicted Values of Freezing Line by Simulation and Experiment and Relative Errors

	freezing length from the fiber cone (mm)			
cone-zone temperature (spin-line profile)	cone-zone T: RT	cone-zone T: 53 °C	cone-zone T: 95 °C	cone-zone T: 115 °C
experiment	7.0 ± 3.2	8.3 ± 1.9	10.3 ± 2.3	14.8 ± 5.1
simulation	6.3	7.6	13.6	20.3
relative error	10%	8%	32%	37%

effect of the surrounding air velocity that is more significant in the case of mode 1 configuration (Figure 2) in which the heater is directly facing the spin line. The direct exposure of the heater creates convective heat movements in the surrounding air of the spin line, which enhances the heat transfer of the jet. Therefore, the experiment results show a relatively smaller freezing length compared to the simulation, as the exact air velocity was not considered in the simulation due to the difficulty of the measurement. The effect of the air velocity was previously mentioned by Joo et al. as electrohydrodynamic quenching.[27]

To understand the effect of the spin-line temperature on the jet viscosity, the temperature of the outer layer of the jet was determined via simulation and is shown in Figure 10a,b (the jet centerline temperature distribution graph along with the 2D images is provided in the Supporting Information Figures S5 and S6). As shown in Figure 10a, the slope of the temperature graph decreases at a distance of about 1 cm from the fiber cone (plateaus). This can be attributed to the start of the phase-change process at this region. The latent heat release during the solidification process slows down the decrease of the temperature along the fiber and lowers the slope of the diagrams. Figure 10b shows the nonsolidified portion of the jet for each of the cases. It is observed that the length of the plateau region is longer at higher spin-line temperature profiles, which highlights the slower heat transfer of the jet inside the higher temperature environment due to the lower temperature gradient. Moreover, on increasing the fiber velocity, we expect

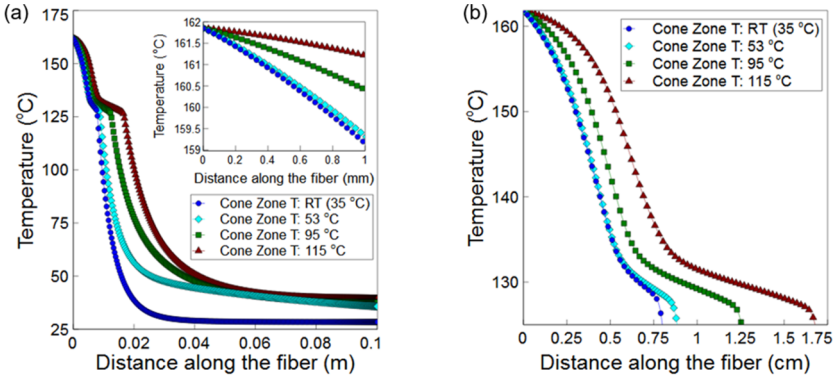

Figure 10. Variation of the fiber temperature at its outer layer for different spin-line air temperature profiles (a) for the full 10 cm length of the jet and (b) the nonsolidified region of the jet.

https://dx.doi.org/10.1021/acsapm.0c01082
ACS Appl. Polym. Mater. 2021, 3, 268−278

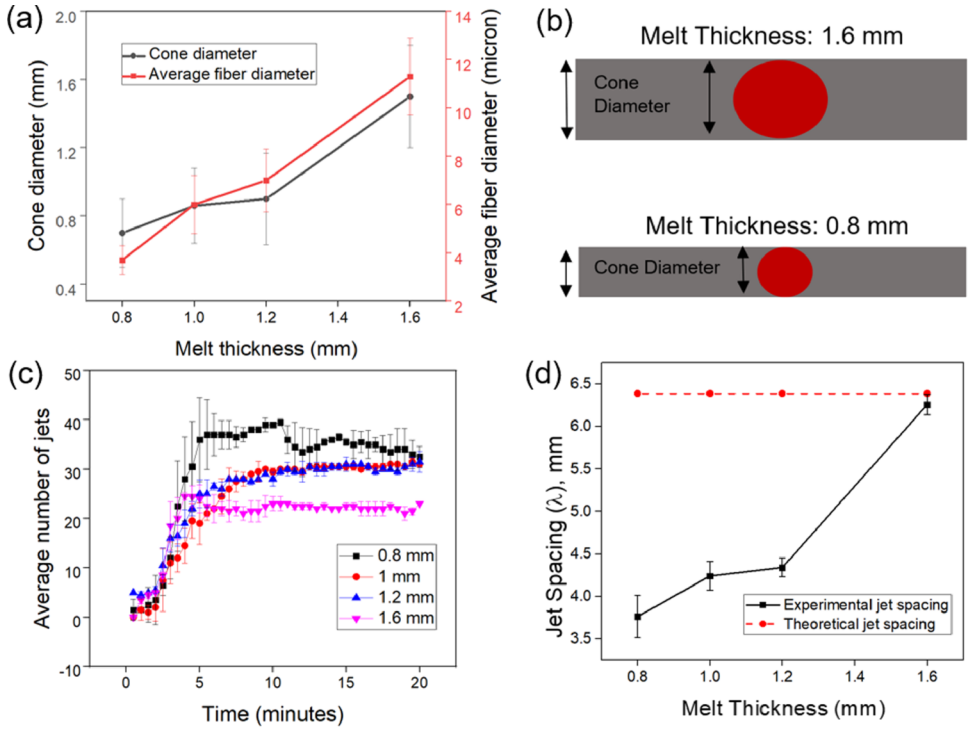

Figure 11. (a) Average cone diameter and fiber diameter vs. four different melt thicknesses, (b) schematic of the cross section of the formed cones from thickness of the polymer melt on the source plate edge, (c) average jet number vs time for four different melt thicknesses, and (d) theoretical and experimental jet spacings for various melt thicknesses. Processing conditions: voltage: 35 kV, distance: 7.5 cm, melt temperature: 165 °C ± 2 at the spin-line temperature profile of 115 °C.

an elongated phase-change region, and therefore, the length of the plateau for the "cone-zone T: 115 °C" is more than others as this case has the highest velocity.

3.5. Lowering Fiber Diameter through Cone Size Adjustment: Regulating Melt Thickness. Unlike the conventional approaches where a nozzle or a spinneret controls the formation of the Taylor cones, in free surface electrospinning, cones are formed freely without confinement. The lack of physical confinement introduces randomness in the cone formation process and signifies the role of the fastest forming instabilities as a result of the interaction of the electric field and surface tension. However, the polymer melt thickness on the plate was identified as a semiphysical confinement parameter, resembling the role of the spinneret in the conventional approaches, which shows a significant effect on the cone and the final fiber diameter as well as the maximum number of the formed cones. The observation shows that the cone diameter decreases with decreasing melt thickness, which ultimately results in a lower fiber diameter (Figure 11a). This is because the formed cones tend to maintain their circular cross section to decrease their surface energy; hence, a lower melt thickness results in a lower cone diameter (Figure 11a,b). The significant decrease in the cone size (by almost twice) leaves more free space between two adjacent cones and this explains the observed higher jet number after 20 min (Figure 11c).

Figure 11c demonstrates that on decreasing the thickness from 1.6 to 0.8 mm, the maximum jet number after 20 min of the process increases to almost twice. The theoretical and experimental jet spacings are calculated and shown in Figure 11d. For various thicknesses, the jet spacing data vary between 3 and 6 mm and are very well correlated with the theoretical results. Based on the theory (eq 9) jet spacing (or jet number) is a function of the electric field and surface tension. However, by changing the melt thickness, it is observed that the jet spacing decreases to almost half the amount. This can be due to excess free space resulting from a smaller cone size in lower melt thicknesses. (it was also previously observed that cone crowdedness lowers the initiated cone diameter).

4. CONCLUSIONS

Controlling the spin-line temperature provides a viable approach to control the fiber morphology including the fiber diameter and uniformity in a melt electrospinning process without the need for direct control over the polymer melt temperature. We reported that a higher spin-line temperature shows an improvement on the maximum jet number and hence increases the production rate and the uniformity of the jet spacings with an enhanced correlation with the theoretical data. Increasing the spin-line temperature from RT up to slightly lower than the polyethylene melting temperature, covering full ranges of the environment temperature possible to attain fibers (above the melting temperature, jets do not solidify in time to form fibers), demonstrated a significant effect on fiber diameter reduction and uniformity of the diameters. We have implemented a unique visual technique of backlighting imaging, which measures the nonsolidified portion (freezing length) of the spinning jet, which was further validated via a numerical simulation.

To elucidate the mechanism of the jet thinning and fiber diameter change with respect to the spin-line temperature, two hypotheses were examined: first, the effect of the cone-zone temperature on the surface tension and subsequently the reduction of the initial cone diameter, as smaller cones produce thinner jets. This hypothesis was ruled out as the visual analysis of the cone diameter both at the initiation and at the final stage of the experiments did not show a trend with the cone-zone

https://dx.doi.org/10.1021/acsapm.0c01082
ACS Appl. Polym. Mater. 2021, 3, 268−278

temperature. The second hypothesis revolved around the jet-dependent parameters including viscosity, jet solidification location, and freezing length. Both the in situ backlit images from the jet in the spin line and the numerical simulation revealed delayed solidification (higher freezing length) at higher spin-line temperatures. We demonstrated that a major portion of the jet in the spin line exists in the solid phase, which does not attribute to any stretchability (not enough chain mobility in the solid phase). Therefore, even an infinitesimal change in the freezing length plays an important role in the jet thinning process, highlighting the role of the translocation of the solidification point on fiber diameter reduction. To investigate the role of viscosity, the jet temperature profile both inside and on the outer layer of the jet was obtained numerically. The temperature of the fully liquid-phase portion of the jet (varies approximately between 0.7 and 1.5 cm for the RT and the 115 °C profiles, respectively) differs to some extent for different spin-line temperature profiles, which proposes the possibility of the viscosity reduction effect on the jet thinning mechanism. The overall observation highlights the overrated importance of the translocation of the solidification point via spin-line temperature adjustment in controlling the fiber morphology, which is mostly overlooked in the literature compared to the other parameters such as melt temperature and viscosity.

In many melt-phase fiber fabrication techniques such as melt spinning, a viable approach to tune the fiber diameter is through increasing the melt temperature largely above the melting point to decrease the viscosity. This approach encompasses limitations due to polymer degradation at prolonged exposure to elevated temperatures as well as the limitation of the critical viscosity to maintain a continuous spinnable jet. The fundamental analysis of the spin-line temperature effect on the solidification point and the subsequent jet thinning that was presented here introduces an alternative approach for fiber morphology attunement in melt-phase fiber fabrication techniques in addition to extending the scope of the melt electrospinning application toward nanofiber fabrication.

■ ASSOCIATED CONTENT

Supporting Information

The Supporting Information is available free of charge at https://pubs.acs.org/doi/10.1021/acsapm.0c01082.

Electric field map, material properties and simulation parameters, theoretical jet spacing analysis, cone diameter analysis, and graphs from COMSOL simulation of the temperature profile along with the phase fraction distribution (PDF)

■ AUTHOR INFORMATION

Corresponding Author

Russell E. Gorga − *Fiber and Polymer Science Program, North Carolina State University, Raleigh, North Carolina 27695, United States;* orcid.org/0000-0002-4416-9532; Email: regorga@ncsu.edu

Authors

Elnaz Shabani − *Fiber and Polymer Science Program, North Carolina State University, Raleigh, North Carolina 27695, United States;* orcid.org/0000-0002-3369-1894

Amir Azimi Yancheshme − *Department of Chemical and Biological Engineering, Drexel University, Philadelphia, Pennsylvania 19104, United States*

Avner Ronen − *Civil and Environmental Engineering Department, Temple University, Philadelphia, Pennsylvania 19122, United States; Zuckerberg Institute for Water Research, The Jacob Blaustein Institutes for Desert Research, Ben-Gurion University of the Negev, Sede Boker 8499000, Israel;* orcid.org/0000-0002-7134-6848

Complete contact information is available at: https://pubs.acs.org/10.1021/acsapm.0c01082

Notes

The authors declare no competing financial interest.

■ ACKNOWLEDGMENTS

This work was partially supported by the "National Science Foundation (NSF)" grant CMMI 1635113. The authors thank Taslim Ur Rashid for his extensive advice on the preparation of this manuscript, Mr. Phillip Strader for assistance with SEM measurements at the AIF center, Rebecca Komer for assistance with the experiments, Chengxi Li for the design of the chamber, Brent Boland for discussion and advice on the electric field simulation, Ms. Birgit Anderson for the differential scanning calorimetry measurements, Mr. Hai Bui for technical assistance with the source plate fabrication, and NC State University libraries for use of digital SLR cameras. The authors would like to acknowledge Dr. Laura Clarke and Dr. Jason Bochinski for their advice.

■ REFERENCES

(1) Bera, B. Literature Review on Electrospinning Process (A Fascinating Fiber Fabrication Technique). *IJIR* **2016**, *2*, 972−984.

(2) Teo, W. E.; Ramakrishna, S. A Review on Electrospinning Design and Nanofibre Assemblies. *Nanotechnology* **2006**, R89.

(3) Wang, C.; Yan, K.-W.; Lin, Y.-D.; Hsieh, P. C. H. Biodegradable Core/Shell Fibers by Coaxial Electrospinning: Processing, Fiber Characterization, and Its Application in Sustained Drug Release. *Macromolecules* **2010**, *43*, 6389−6397.

(4) Ye, P.; Xu, Z.-K.; Wu, J.; Innocent, C.; Seta, P. Nanofibrous Membranes Containing Reactive Groups : Electrospinning from Poly (Acrylonitrile-Co-Maleic Acid) for Lipase Immobilization. *Macromolecules* **2006**, *39*, 1041−1045.

(5) Gentsch, R.; Pippig, F.; Schmidt, S.; Cernoch, P.; Polleux, J.; Hans, G. B. Single-Step Electrospinning to Bioactive Polymer Nanofibers. *Macromolecules* **2011**, *44*, 453−461.

(6) Ma, M.; Mao, Y.; Gupta, M.; Gleason, K. K.; Rutledge, G. C. Superhydrophobic Fabrics Produced by Electrospinning and Chemical Vapor Deposition. *Macromolecules* **2005**, *38*, 9742−9748.

(7) Shi, X.; Xu, Z.; Huang, C.; Wang, Y.; Cui, Z. Selective Swelling of Electrospun Block Copolymers : From Perforated Nanofibers to High Flux and Responsive Ultrafiltration Membranes. *Macromolecules* **2018**, *51*, 2283−2292.

(8) Laforgue, A.; Robitaille, L. Production of Conductive PEDOT Nanofibers by the Combination of Electrospinning and Vapor-Phase Polymerization. *Macromolecules* **2010**, *43*, 4194−4200.

(9) Long, Y.; Chen, H.; Yang, Y.; Wang, H.; Yang, Y.; Li, N.; Li, K.; Pei, J. Electrospun Nanofibrous Film Doped with a Conjugated Polymer for DNT Fluorescence Sensor. *Macromolecules* **2009**, *42*, 6501−6509.

(10) Yarin, A. L.; Zussman, E. Upward Needleless Electrospinning of Multiple Nanofibers. *Polymer* **2004**, *45*, 2977−2980.

(11) Lukas, D.; Sarkar, A.; Pokorny, P. Self-Organization of Jets in Electrospinning from Free Liquid Surface: A Generalized Approach. *J. Appl. Phys.* **2008**, *103*, 084309.

(12) Chen, H.; Li, H.; Ma, X.; He, W.; Tan, J.; Yang, W. Large Scaled Fabrication of Microfibers by Air-Suction Assisted Needleless Melt Electrospinning. *Fibers Polym.* **2016**, *17*, 576−581.
(13) Thoppey, N. M.; Gorga, R. E.; Bochinski, J. R.; Clarke, L. I. Effect of Solution Parameters on Spontaneous Jet Formation and Throughput in Edge Electrospinning from a Fluid-Filled Bowl. *Macromolecules* **2012**, *45*, 6527−6537.
(14) Forward, K. M.; Flores, A.; Rutledge, G. C. Production of Core/Shell Fibers by Electrospinning from a Free Surface. *Chem. Eng. Sci.* **2013**, *104*, 250−259.
(15) Fang, J.; Zhang, L.; Sutton, D.; Wang, X.; Lin, T. Needleless Melt-Electrospinning of Polypropylene Nanofibres. *J. Nanomater.* **2012**, *2012*, 382639.
(16) Thoppey, N. M.; Gorga, R. E.; Clarke, L. I.; Bochinski, J. R. Control of the Electric Field-Polymer Solution Interaction by Utilizing Ultra-Conductive Fluids. *Polymer* **2014**, *55*, 6390−6398.
(17) Roman, M. P.; Thoppey, N. M.; Gorga, R. E.; Bochinski, J. R.; Clarke, L. I. Maximizing Spontaneous Jet Density and Nanofiber Quality in Unconfined Electrospinning: The Role of Interjet Interactions. *Macromolecules* **2013**, *46*, 7352−7362.
(18) Komárek, M.; Martinová, L. Design And Evaluation Of Melt-Electrospinning Electrodes. *Nano* **2010**, *10*, 12−14.
(19) Ko, J.; Mohtaram, N. K. Principle and Equipment of Polymer Melt Differential Electrospinning Preparing Ultrafine Fiber. *Nano* **2014**, *64*, No. 012013.
(20) Wang, Q.; Curtis, C. K.; Thoppey, N. M.; Bochinski, J. R.; Gorga, R. E.; Clarke, L. I. Unconfined, Melt Edge Electrospinning from Multiple, Spontaneous, Self-Organized Polymer Jets. *Mater. Res. Express* **2015**, *1*, 45304.
(21) Góra, A.; Sahay, R.; Thavasi, V.; Sahay, R. Melt-Electrospun Fibers for Advances in Biomedical Engineering, Clean Energy, Filtration, and Separation. *Polym. Rev.* **2011**, *51*, 265−287.
(22) Brown, T. D.; Dalton, P. D.; Hutmacher, D. W. Melt Electrospinning Today: An Opportune Time for an Emerging Polymer Process. *Prog. Polym. Sci.* **2016**, *56*, 116−166.
(23) Morikawa, K.; Vashisth, A.; Grimme, C. J.; Green, M. J.; Naraghi, M. Wire Melt Electrospinning of Thin Polymeric Fibers via Strong Electrostatic Field Gradients. *Macromol. Mater. Eng.* **2019**, *304*, 1−9.
(24) Thoppey, N. M.; Bochinski, J. R.; Clarke, L. I.; Gorga, R. E. Unconfined Fluid Electrospun into High Quality Nanofibers from a Plate Edge. *Polymer* **2010**, *51*, 4928−4936.
(25) Liu, Z.; Li, H.; Wu, W.; Chen, H.; Ding, Y.; Yang, W. Effect of Electric Field on Gas-Assisted Melt Differential Electrospinning with Hollow Disc Electrode. *J. Polym. Eng.* **2015**, *35*, 61−70.
(26) Mayadeo, N.; Morikawa, K.; Naraghi, M.; Green, M. J. Modeling of Downstream Heating in Melt Electrospinning of Polymers. *J. Polym. Sci. Part B: Polym. Phys.* **2017**, *55*, 1393−1405.
(27) Zhmayev, E.; Cho, D.; Joo, Y. L. Electrohydrodynamic Quenching in Polymer Melt Electrospinning. *Phys. Fluids* **2012**, *23*, No. 073102. September 2010
(28) Shabani, E.; Rashid, T. U.; Gorga, R. E.; Krause, W. E. A Facile LED Backlight in Situ Imaging Technique to Investigate Sub-Micron Level Processing. *Polym. Test.* **2020**, *92*, 106865.
(29) Alawadhi, E. M.; Amon, C. H. PCM Thermal Control Unit for Portable Electronic Devices: Experimental and Numerical Studies. *IEEE Trans. Comp. Packag. Technol.* **2003**, *26*, 116−125.
(30) Mzad, H.; Otmani, A.; Bey, K.; Łopata, S. A Model of Water-Spray Cooling Effect on a Continuous Casting Process. *MATEC Web Conf.* **2018**, *240*, No. 05022.
(31) Matsuo, T.; Kase, S. Studies on Melt Spinning . VII . Temperature Profile. *J. Appl. Polym. Sci.* **1976**, *20*, 367−376.
(32) Capone, C.; Di Landro, L.; Inzoli, F.; Penco, M.; Sartore, L.; Vinci, L. Thermal and Mechanical Degradation During Polymer Extrusion Processing. *Polym. Eng. Sci.* **2007**, *47*, 1813−1819.
(33) Stutz, H.; Pionteck, J.; Pötschke, P. Surface Tension, Interfacial Tension , and Morphology in Blends of Thermoplastic Polyurethanes and Polyolefins. Part I . Surface Tension of Melts of TPU Model Substances and Polyolefins. *Polymer* **2002**, *43*, 6965−6972.

https://dx.doi.org/10.1021/acsapm.0c01082
ACS Appl. Polym. Mater. 2021, 3, 268−278